11th International Workshop on Ship and Marine Hydrodynamic
Hamburg, Germany, September 22-25, 2019

Numerical Analysis of A Floating Horizontal Axis Tidal Current Turbine with Sway Motion

C. Zeng*, **M. Abdel-Maksoud**

Hamburg University of Technology, Institute for Fluid Dynamics and Ship Theory
Am Schwarzenberg-Campus 1, 21073 Hamburg, Germany

*Corresponding author, chen.zeng@tuhh.de

ABSTRACT

Increasing the rotational speed of a turbine rotor leads to a reduction of the stream velocity passing through the rotor. By diverging the upstream flow, the slowed wake reduces the fluid mass flowing through the rotor, and thus, the power output. The present study aims to determine if and by which extent a sway motion, by deviating the turbine rotor from the following delayed wake, is able to improve the power output of a turbine. A low-order panel method, namely *pan*MARE, is applied, and the DOE Reference Model 1 turbine is used as the test object. First, a series of open-water simulations is carried out and compared with the corresponding RANS results to verify the numerical setup. Then, the hydrodynamic behaviour of a turbine swaying sinusoidally with two different time periods are simulated. The results indicate that the sway motion does help to improve the power harness of the turbine and the improvement increases with the increase of the maximum sway velocity as well as the tip speed ratio of the turbine rotor. Some other characteristics of the turbine in sway motions are also investigated by the subsequent data analysis.

(Keywords: Tidal current turbine, Sway motion, Panel method, Betz limit, Wake)

1 INTRODUCTION

Tidal kinetic energy has become increasingly more interesting due to its huge potential and a high degree of predictability. Further, horizontal-axis turbines, which have long-term operational experience in the wind turbine industry, have been configured together with tidal energy devices, for example, in the horizontal-axis tidal current turbine (HATT).

A turbine in free space is restricted by Betz limit [1], which states that a single isolated turbine has a maximum power coefficient Cp=16/27. For the reason that, with the increase of tip speed ratio (TSR), the stream passing through a turbine is decelerated more and more. The slowed fluid diverges the upstream flow that reduces the fluid mass going through the rotor disc. Thus, the stream kinetic energy harnessed by the turbine is reduced when its TSR exceeds the optimum value [2].

Unlike typical wind turbines, there are some approaches for a HATT to have a power coefficient exceeding Betz limit. As introduced by Vennell et al. [3], when grouping turbines into a large farm in tidal channels with fast inflow, the divergence of the stream through a turbine rotor is restricted by adjacent rotor (called 'blockage effect') with the help of other boundaries such as sea bed and water surface. Thus, a turbine will harvest kinetic energy from a greater mass of fluid and its power output is improved [4].

Therefore, it is useful to investigate the possibility of a single HATT to improve its power output in a relatively open space. In the present study, sinusoidal sway motion with different time period is actively induced to a HATT in order to deviate the turbine from its delayed wake to reduce the negative influence on the upstream flow.

The study is based on the three-dimensional low-order panel solver *pan*MARE. A HATT rotor model called DOE Reference Model 1 (DOE RM1) is chosen as the object. DOE RM1 is a 2-bladed HATT rotor with a diameter of 20 meters. The rotor is developed by the National Renewable Energy Laboratory of the United States (NREL) [5]. After the grid study, three *pan*MARE simulations are carried out to compare with the RANS simulation conducted by the turbine developers. Then, the single rotor DOE RM1 turbine with sway motion is simulated with *pan*MARE to study the performance of the turbine in sway motion.

2 METHODOLOGY

*pan*MARE is an in-house hydrodynamic solver, dedicated to marine applications, based on low-order three-dimensional panel method [6].

2.1 Basic potential theory

The procedure applied in *pan*MARE is close to the approach developed by Katz and Plotkin [7]. The total velocity of an incompressible fluid q can be described as the combination of inflow velocity V_∞ and induced velocity u: $q = V_\infty + u$. When a body is moving, the velocity induced by the motion is incorporated in V_∞. Assuming the flow field of u is irrotational, the induced velocity can be represented as $u = \bigtriangledown\phi$. Also, the induced potential satisfies the Laplace equation $\bigtriangledown^2\phi = 0$, which can be applied to the body surface to calculate the velocity potential. At each panel collocation point, the value of potential and its derivative in normal direction are referred to doublet strength $\mu = -\phi$ and source strength $\sigma = \bigtriangledown\phi\cdot\vec{n}$.

The wake surface, which has no thickness, is applied to model the vorticity shedding from the body and it is crucial for the accurate description of the flow field [8], [10]. The linear Kutta condition is applied in the simulation that the difference of doublet strength of the body panels on both sides of trailing edge equals to the doublet strength of the first wake panel downstream of the trailing edge.

As a non-negligible factor for torque calculation of a HATT, the friction is estimated by Schoenherr equation [9]. The equation calculates the local, turbulent friction coefficient ($C_{\tau,turb}$) as follows:

$$C_f = \frac{1}{(3.46 \cdot log_{10}(R_x) - 5.6)^2} \tag{1}$$

$$C_{\tau,turb} = \frac{C_f}{1 + 3.56 \cdot \sqrt{C_f}} \tag{2}$$

where R_x is local Reynolds number and C_f is the coefficient of skin-frictional resistance.

2.2 Wake alignment method

A wake alignment method is an iterative procedure to enforce the wake locally to be tangential to the flow direction. An unsteady method is used in *pan*MARE, which is introduced by Wang [8]. The position of converged wake nodal point should satisfy:

$$\frac{d\boldsymbol{x}}{dt} = \boldsymbol{q}(\boldsymbol{x}) \tag{3}$$

among which $\boldsymbol{x}$ stands for the wake nodal point position and $\boldsymbol{q}(\boldsymbol{x})$ the total velocity.

The aforementioned equation can be solved in the unsteady wake alignment method with the application of the Euler-Forward scheme. The solution is displayed as follows:

$$\boldsymbol{x}_{i+1}^{n+1} = \boldsymbol{x}_i^n + \boldsymbol{q}(\boldsymbol{x}_i^n)\Delta t \tag{4}$$

where the subscripts represent the row indexes, while the superscripts stand for the number of iteration steps.

3 VERIFICATION

3.1 Simulation setup

As a variable-speed variable-pitch (VSVP) turbine, the developers [5] determined the variation of the rotation speed and the blade's pitch angle with respect to the free stream velocity from 0.5 m/s to 3.0 m/s. Among the range, they chose three underrated operating conditions to carry out RANS simulations; the details of these operating conditions are listed in Table 1 [5]. In order to compare with the existing RANS results, *pan*MARE simulations are carried out with the same operating condition.

Table 1: Turbine operating conditions simulated with STAR-CCM+ by NREL. [5]

Operating condition	Flow vel. (m/s)	Rotor spd. (rpm)	Blade pitch (deg)
A	1.0	6.68	0
B	1.5	10.03	0
C	1.9	11.50	0

The circular cross-section at the root of DOE RM1 blade, enabling the blade-pitching mechanism, is transitioned to the airfoil of NACA 63(1)-424 at 20% of the blade span; see the left side of Figure 1. For the restriction in panel method by simulating separated flows, the blade segments with oval-like cross sections are excluded, which is displayed in the right side of Figure 1.

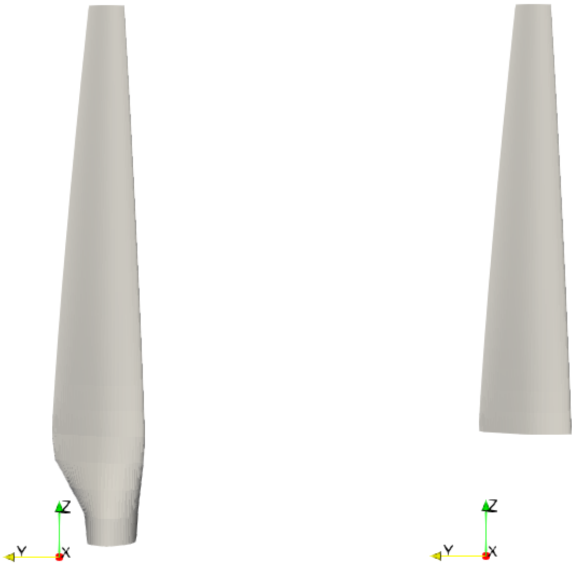

Figure 1: DOE-RM1 blade geometries.

3.2 Grid study

A grid study for the operating condition B is performed to determine a reasonable grid resolution. Three grids, coarse, medium and fine, are generated and displayed in Figure 2. In these grids, the ratio between the radial and chord-wise resolutions is kept constant, as well as the refinement functions.

According to Table 2, the deviation of the results decreases to the fine mesh results with the increase of grid resolution. Compared to the coarse mesh, the medium mesh has a better convergence to the fine mesh as well as a more accurate description of the blade geometry. Also, it demands much less computing effort than fine mesh does. The medium mesh is utilized in the following simulations.

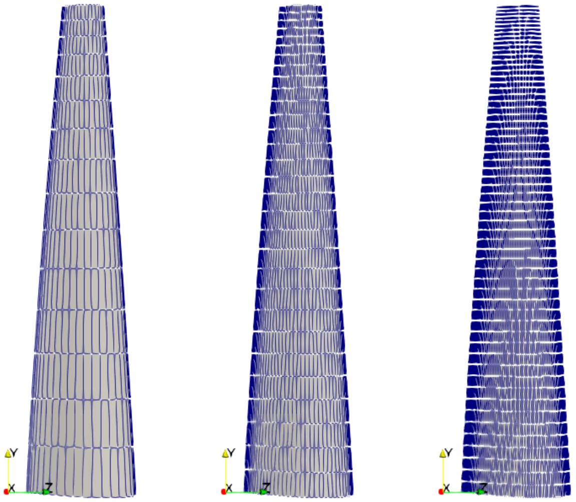

Figure 2: Coarse grid, medium grid and fine panel grid from left side to right side.

Table 2: Difference from fine grid result.

Grid	ΔTorque (%)	ΔThrust (%)
Coarse	2.41	0.95
Medium	1.23	0.15
Fine	-	-

3.3 Results

The comparison of the HATT torques derived by three different hydrodynamic simulators, WT_Perf, STAR-CCM+ as well as *pan*MARE , are displayed in the left sub-figure of Figure 3. The simulations by WT_Perf, a BEMT code, and STAR-CCM+, a RANS code, are carried out by Lawson [5]. The *pan*MARE results show good agreement with the WT_Perf curve. When compared to the results from the RANS simulation, every point obtained by *pan*MARE shows an underestimation of around 12%; see Table 3.

Table 3: Torque differences between simulations.

Operating condition	Torque ($kN \cdot m$)		Difference (%)
	STAR-CCM+	*pan*MARE	
A	113.5	100.6	11.5
B	256.1	225.2	12.1
C	449.4	395.6	12.0

To gain an insight into the difference between the *pan*MARE and RANS simulations, the torque distributions along the blade, when the turbine operates under the condition C, are sketched as can be seen in Figure 3. It can be observed that the results from *pan*MARE show good agreement with that from STAR-CCM+. By integrating the red curve from the root to where the blade is cut in the *pan*MARE simulation, it can be seen that the shrink part contributes approximately 7% of the total torque. This indicates that the local differences between the panel and RANS results may not be as big as what is shown in Table 3 for global values. Thus, it may be concluded that the current *pan*MARE setups are suitable for the following simulations.

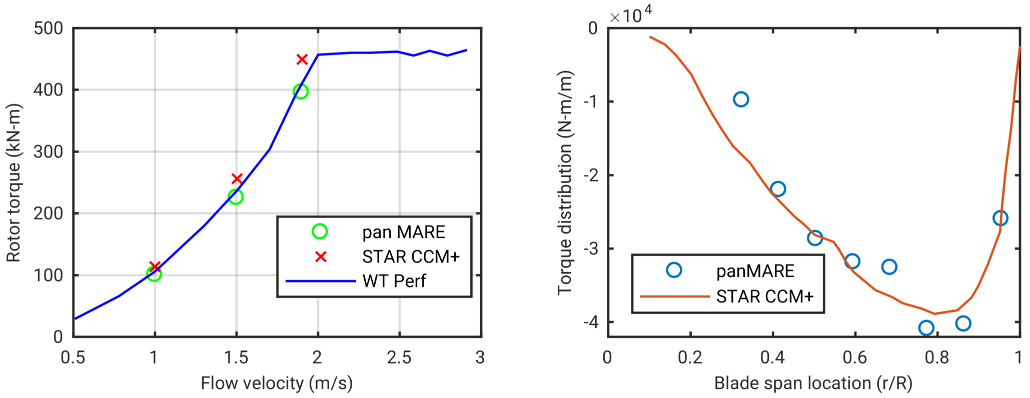

Figure 3: Comparison of rotor torques and sectional torque distributions.

4 SIMULATION OF THE SINGLE ROTOR DOE RM1 TURBINE WITH SWAY MOTION

4.1 Parameters of simulation

The free-stream velocity of the operating condition B, $V = 1.5m/s$, is used in the subsequent simulations. Sway motion for two time periods, 120 second and 240 seconds, is induced to the DOE RM1 turbine. Both of them have the same displacement amplitude equalling to $20m$, which is also the turbine diameter. At the same phase angle, the turbine sways with the time period of 120 seconds twice as fast as that of 240 seconds. Thus, the influence of sway velocity amplitude can be analysed. With each time period of sway, simulations are carried out with the turbine rotating at a series of TSRs in a range from 5 to 9. TSRs are calculated with the equation below:

$$TSR = \frac{\omega * R}{V} \tag{5}$$

where ω is the angular velocity of the turbine and R the rotor radius and V the free-stream velocity.

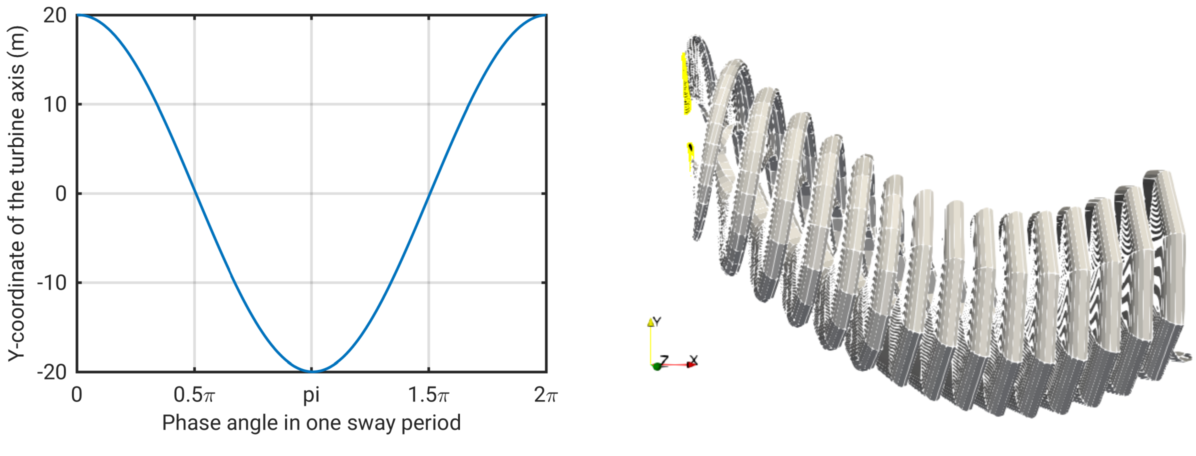

Figure 4: Location of the turbine axis in one sway period and a screen shot of a swaying turbine.

The y-direction movement of the turbine is displayed in the left Figure 4 and the right side shows the screen-shot of a swaying turbine in *pan*MARE simulation. The other simulation setups are in accordance with that of the previous verification.

Power and thrust coefficients for the DOE RM1 turbine with sway motion are calculated as follows:

$$C_P = \frac{P}{0.5\rho A V^3} \tag{6}$$

$$C_T = \frac{T}{0.5\rho A V^2} \tag{7}$$

where P and T represent power and thrust respectively. A is the area of the HATT rotor disc.

4.2 Comprehensive performance of the turbine in sway motion

To evaluate the comprehensive performance of the DOE RM1 turbine with sinusoidal sway motions, average power and thrust coefficients of the turbine in one sway period are plotted on Figure 5 with respect to TSR ranges from 5 to 9. As can be seen from the figures, at each rotational speed, the power and thrust coefficients from swaying simulations are higher than that of the steady case, which proves that sway motion is able to improve the power converted by the turbine.

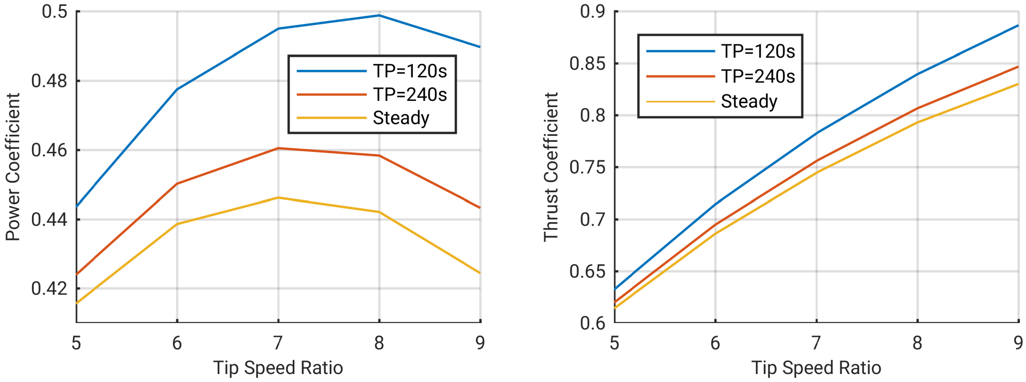

Figure 5: Mean power and thrust coefficient as a function of tip speed ratio for a single rotor DOE RM1 turbine with and without sway motions.

Several trends can be observed from the figures. First, the power and thrust coefficients increase with the decrease of the time period of sway motion, i.e. the increase of sway velocity. Secondly, the increment of power coefficient due to sway motion increases with the turbine rotational speed, i.e. TSR. Furthermore, the optimum TSR value, where the power coefficient reaches its maximum, rises with a decrease of swaying time period.

The trends conform to the expectations that the higher velocity a turbine sways, the better ability it could acquire to deviate from its original wake. Therefore, more fluid mass may pass through the turbine and lead to a higher power coefficient. As mentioned in the introduction, the divergence of fluid mass plays a more important role in confining power harness by a HATT when it rotates at a high speed. This may be the reason that sway motion works more efficiently in the high TSR region.

4.3 Variation of the thrust and power coefficients over one sway period

The power and thrust coefficient with respect to the phase angle in one sway period are displayed in the figures of Appendix A. Five sets of figures with the TSR increasing from 5 to 9 are displayed . In each set, the turbine rotor rotates at the same TSR. There are two oscillating curves and one line displayed in each of the figures; the curves represent power or thrust coefficient of the turbine sways with different time periods while the line is from the reference simulation without sway motion.

There are some commonalities in these figures. Over the whole sway period, the turbine in sway simulations shows higher power and thrust coefficient than it does in steady simulations. And with a smaller time period, i.e. higher sway velocity, it shows further increase in coefficients. It can also be observed that every coefficient curve oscillates with two major frequencies; one is much smaller than the other. Hence, it can be assumed that the coefficient oscillation, induced by the sinusoidal sway motion, is composed of two oscillations with different frequencies. According to their difference in value, the frequencies are called low-frequency (LF) and high-frequency (HF).

The LF is twice as much as that of the sway motion and the amplitude LF oscillation is constant through a sway period. The highest value of LF oscillation is close to the phase angle when the turbine returns to neutral position where the sway velocity reaches its maximum, while the lowest value appears when the sway velocity is almost zero. It may indicate that LF oscillation is mainly influenced by the changes of sway velocity.

When it comes to HF oscillation, the frequency doubles the blade rotational frequency. The amplitude of HF oscillation varies over a sway time period, which increases and decreases with sway speed. When the turbine sways, the two rotating blades will have different locations to the induced lateral flow. And the location difference varies periodically with the double frequency of the blade rotation, which coincides with HF. It can be assumed that the different flow conditions around the two blades mean that the pressure distribution on the surface of a blade is asymmetric to the other. The varying differences in pressure distribution on the blades may be the reason for the minor disturbance (HF oscillation).

Further, it can be stated that both LF and HF oscillations show an increase in amplitude with increasing rotational speed of the turbine by comparing the figures in Appendix A.

4.4 Analysis of each blade

The differences in pressure distribution on each blade may lead to HF oscillation. To examine the performance differences of the two blades in swaying motion, these two time instants are analysed. These time instants are derived from the simulation with the most significant sway influence. The turbine in the chosen simulation rotates at the TSR of 9 and sways with a time period of 120 seconds. As displayed in Figure 6, the power and thrust coefficient meets a global maximum at time instant A and followed by a local minimum at time instant B.

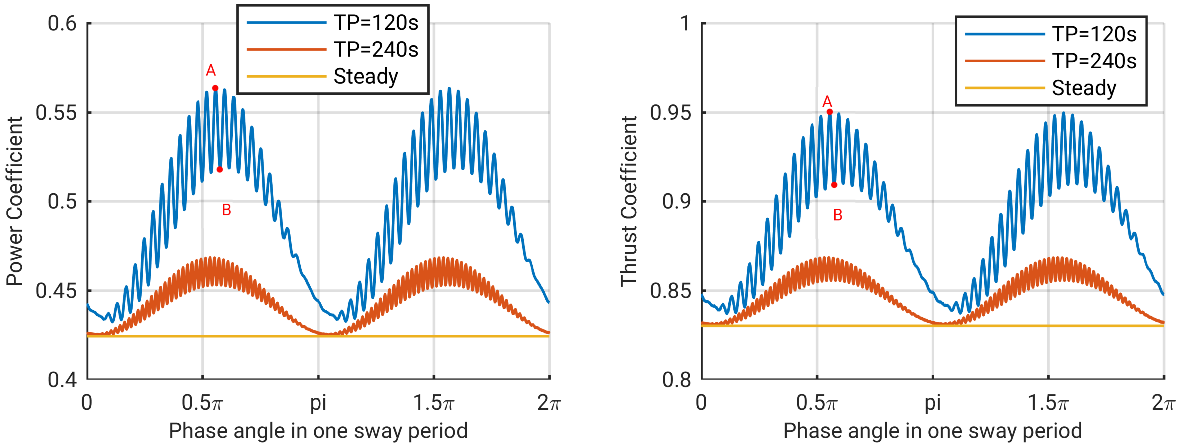

Figure 6: Comparison of power and thrust coefficient of a single rotor DOE RM1 turbine with respect to phase angle in one sway period. TSR=9

The turbine in both subfigures of Figure 7 sways towards the negative Y-direction and the left subfigure shows the turbine at time instant A, and the turbine at time instant B is displayed in the right subfigure. It can be noticed that when the sway velocity keeps constant, the DOE RM1 turbine harvests the highest amount of power when the blades are parallel to the Y-axis; while the power coefficient reaches its local minimum when the blades rotates to the vertical position.

The torques contributed by Blade 1 and Blade 2 at the time instants (see Figure 8) are listed in Table 4. At time point A, Blade 1 produces significantly higher torque than the other blade. Then, the torque of Blade 1 experiences a reduction while the torque from Blade 2 slightly decreases during the

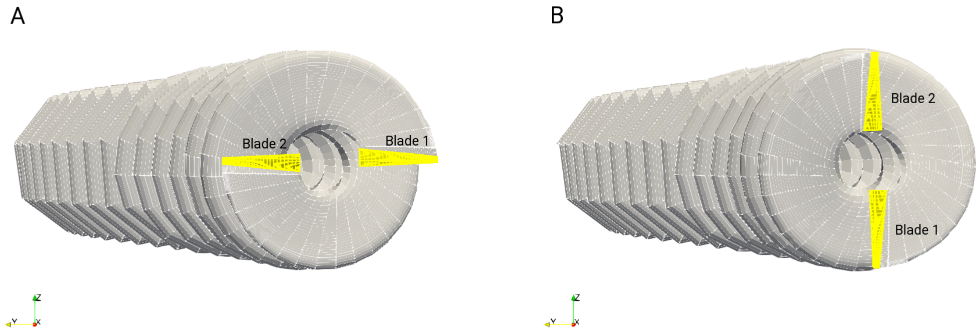

Figure 7: The locations of the turbine at the two time instants.

rotor rotates to the position of time instant B.

Table 4: Blade torque of the power coefficient at time instant A and B.

Time Instant	Torque of Blade 1	Torque of Blade 2
A	128.9	91.5
B	113.5	89.1

The radial torque distribution on each blade is plotted in Figure 8. From the figure, significant changes in radial torque distribution between these time instants can be noticed. At both time instants, radial torque distributed on Blade 1 has a higher maximum value than the torque on Blade 2. When the turbine rotor rotates from time instant A to time instant B, the torque distribution in larger radius region of Blade 1 meets a significant decline, yet the torque distributed in smaller radius region slightly increases. When it comes to Blade 2, the torque distribution in larger radius part is increased and the other blade region experiences a substantial decrease in torque distribution. With consideration of the differences in the turbine rotor displayed in both subfigures of Figure 7, the changes of the blade location in relation to the wake may lead the variation of the torque distribution.

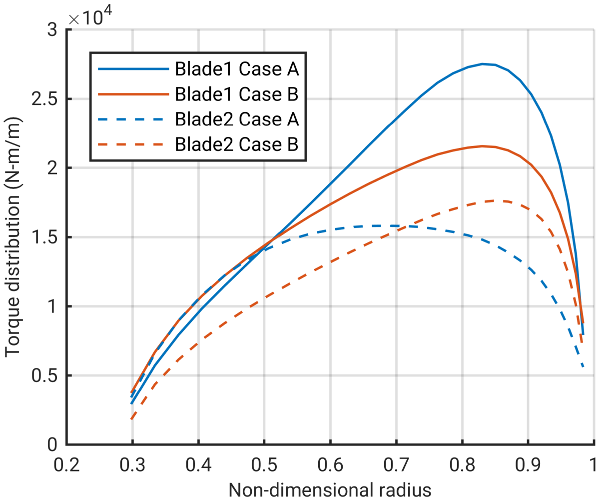

Figure 8: Radial torque distribution over one blade.

The velocity diagram relating to a blade cross-section is presented in Figure 9. In the figure, U_F

and U_I represents the free stream velocity and the induced axial velocity. V_S is the tangential velocity due to sway motion and V_I is the induced tangential velocity. ΩR represents the tangential velocity of the blade cross-section caused by the rotor rotation. By composing the aforementioned velocities, the resultant velocity is:

$$V = \sqrt{(U_F + U_I)^2 + (V_I + V_S + \Omega R)^2} \tag{8}$$

Respectively, θ, ϕ and α are twist-angle of the cross-section, incoming flow direction angle and angle of attack.

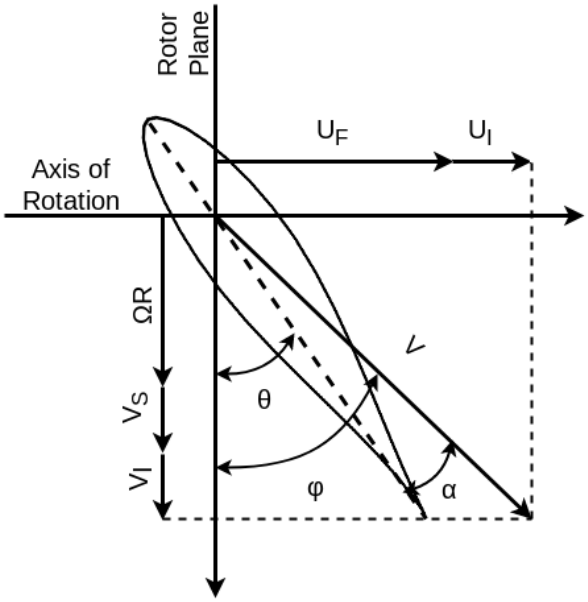

Figure 9: Velocities relating to the airfoil.

Table 5: Some velocities in the diagram.

	Time Instant A		Time Instant B	
	Blade 1	Blade 2	Blade 1	Blade 2
V_S	0	0	-1.041	1.041
U_F	1.5	1.5	1.5	1.5

The values of V_S and U_F are listed in Table 5, and the induced velocity with respect to the radial position of the cross-section is displayed in Figure 10. The plotted induced velocity is the average of the induced fluid velocity located at $0.5m$ upstream of the cross-section, which is mainly influenced by the wake. Then, the angle of attack, as well as the resultant velocity, are calculated in accordance with the aforementioned diagram and equation. The results are presented in Figure 11. At both time instants, U_F and ΩR are constant at the same radial position on both blades. Thus, the differences in the flow around each blade may be mainly caused by U_I, V_I as well as V_S.

According to the diagram, the angle of attack increases with the increase of the total axial fluid velocity while decreases with the increase of the total tangential flow speed. Based on the left sub-figures of Figure 7 and Figure 10, it can be concluded that the wake has a strong influence on the changing of axial fluid velocity. The upstream axial fluid speed decelerated greatly when the blade located in front of the overlapped wake panels (Blade 2 Case A). When the blade is away from the accumulated wake panels (Blade 1 Case A), the axial fluid speed has a much less reduction. Compared to the other tangential velocities, the tangential induced velocity is small; thus it may have limited influence on the calculation of the angle of attack. When it comes to time instant B, V_S is negative for Blade 1 and positive for Blade

2. Therefore, the tangential velocity induced by the sway motion increases the angle of attack of Blade 1 while decreases that of Blade 2 at the time instant. In conclusion, the angle of attack can be influenced by the relative position of the blade to wake as well as directly by the sway motion.

From the right subfigure in Figure 11, it may be concluded that the change of resultant fluid velocity is mainly influenced by the tangential fluid speed induced by the sway motion. It can be derived from the following facts. The resultant fluid velocity of both blades almost shows no difference at time instant A when V_S keeps zero for both blades. While at time instant B, when V_S for Blade 1 is equal to the negative sway velocity while it is positive for Blade 2, the resultant velocity of the latter is significantly higher than the velocity of the former.

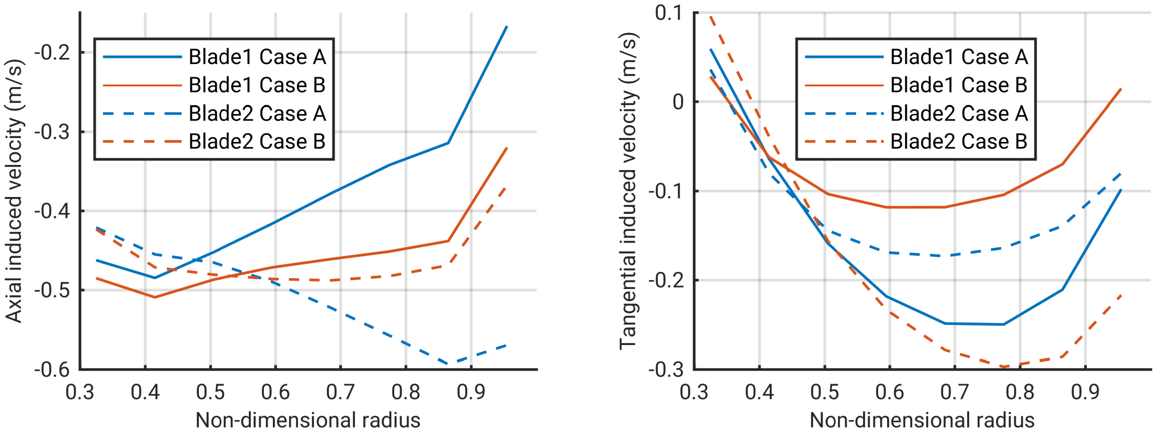

Figure 10: Distribution of axial and tangential induced velocity on one blade.

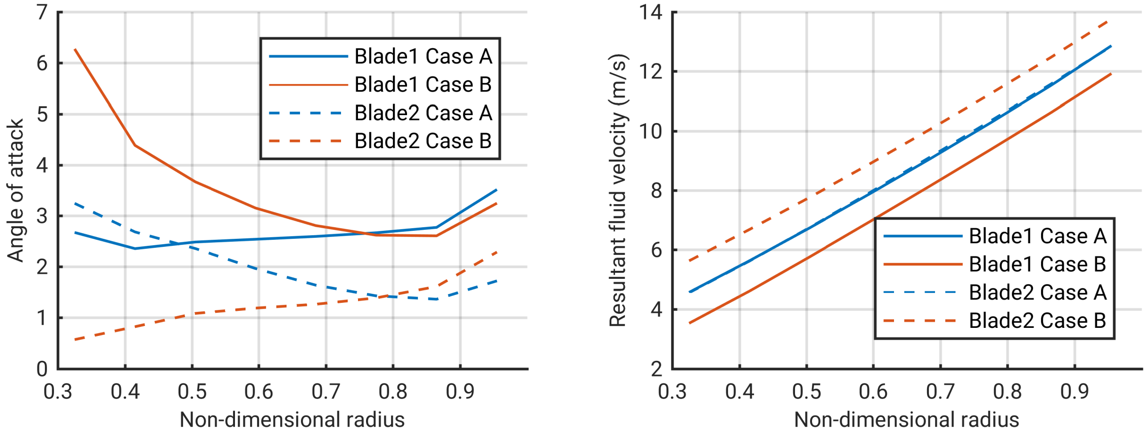

Figure 11: Variation of angle of attack and resultant fluid velocity over one blade.

4.5 Lateral hydrodynamic force

The hydrodynamic lateral force may be a major sway resistance. With respect to TSR, the root-mean-square of the lateral forces in one sway period are plotted in Figure 12. From the figure, lateral forces show a downward trend with the increase of rotational speed, no matter how long the time period is. And the mean value of lateral force is remarkably small compared to the mean value of thrust, which is only about 1% of the latter.

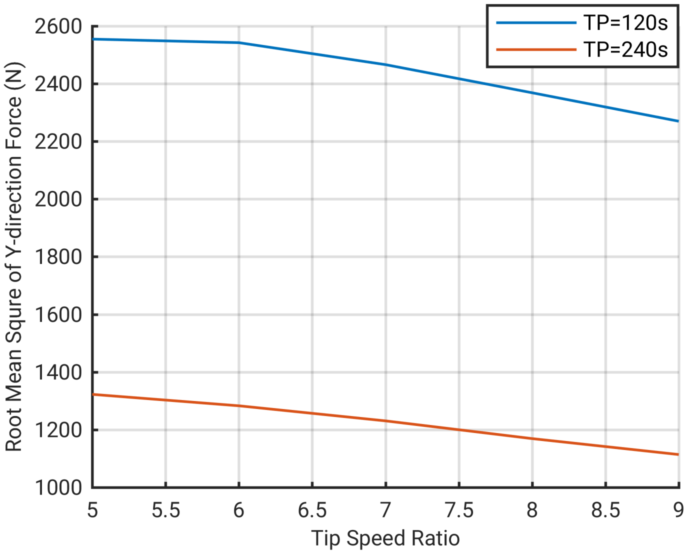

Figure 12: Root mean square lateral force of the turbine.

5 CONCLUSION AND FUTURE WORK

The DOE RM1 turbine swaying sinusoidally with two different time periods are simulated with respect to a series of TSRs. The results indicate that the sway motion does help increase the tidal kinetic energy harnessed by the HATT. The power improvement due to the sway motion increases with the sway velocity as well as the tip speed ratio of the turbine.

When it comes to the performance of the turbine in one sway period, each coefficient mainly oscillates at two different frequencies. Carrying out the Fast Fourier analysis, it can be concluded that the power or thrust coefficient oscillation with a lower frequency may be caused by the varying of sway velocity whilst the oscillation with a high frequency is mainly influenced by the changing of the flow around both blades. We may conclude that the performance of a blade is highly influenced by its relative position to the wake and the lateral flow. With the analysis of the lateral hydrodynamic force, the root-mean-square of the force decreases with the TSR, and surprisingly, the resistance is remarkably small when comparing to the thrust.

In the future, a twin-rotor turbine, with which configuration the large torque of HATT could be canceled, will be simulated with forced sway motion and free-motion model. The mechanism to induce the sway motion will also be studied.

ACKNOWLEDGEMENTS

The first author is sponsored by the China Scholarship Council (201608060390).

REFERENCES

[1] A. Betz. “Das Maximum der theoretisch möglichen Ausnutzung des Windes durch Windmotoren”. In: *Zeitschrift fur das gesamte Turbinenwesten* 20 (1920).

[2] J. F. Manwell, J. G. McGowan and A. L. Rogers. *Wind Energy Explained*. Wiley John + Sons, 2010. 704 pp.

[3] R. Vennell. “Exceeding the Betz limit with tidal turbines”. In: *Renewable Energy* 55 (2013), pp. 277–285.

[4] P. L. Fraenkel. “Power from marine currents”. In: *Proceedings of the Institution of Mechanical Engineers, Part A: Journal of Power and Energy* 216.1 (2002), pp. 1–14.

[5] M. J. Lawson, Y. Li and D. C. Sale. “Development and verification of a computational fluid dynamics model of a horizontal-axis tidal current turbine”. In: *ASME 2011 30th International Conference on Ocean, Offshore and Arctic Engineering.* American Society of Mechanical Engineers. 2011, pp. 711–720.

[6] M. Bauer and M. Abdel-Maksoud. “A Three-Dimensional Panel Method for the Simulation of Sheet Cavitation in Marine Propeller Flows”. In: *PAMM* 12.1 (2012), pp. 743–744.

[7] J. Katz and A. Plotkin. *Low-speed aerodynamics.* Vol. 13. Cambridge Aerospace Series. Cambridge, United Kingdom: Cambridge University Press, 2001.

[8] Y. Wang, M. Abdel-Maksoud and B. Song. “Convergence of different wake alignment methods in a panel code for steady-state flows”. In: *Journal of Marine Science and Technology* 21.4 (2016), pp. 567–578.

[9] S. Hoerner. *Fluid-dynamic drag: practical information on aerodynamic drag and hydrodynamic resistance.* Hoerner Fluid Dynamics, 1965.

[10] Y. Wang, M. Abdel-Maksoud, K. Wang and B. Song. “Prediction of tip vortex cavitation inception with low-order panel method”. In: *Ocean Engineering* 125 (2016), pp. 124–133.

A APPENDIX

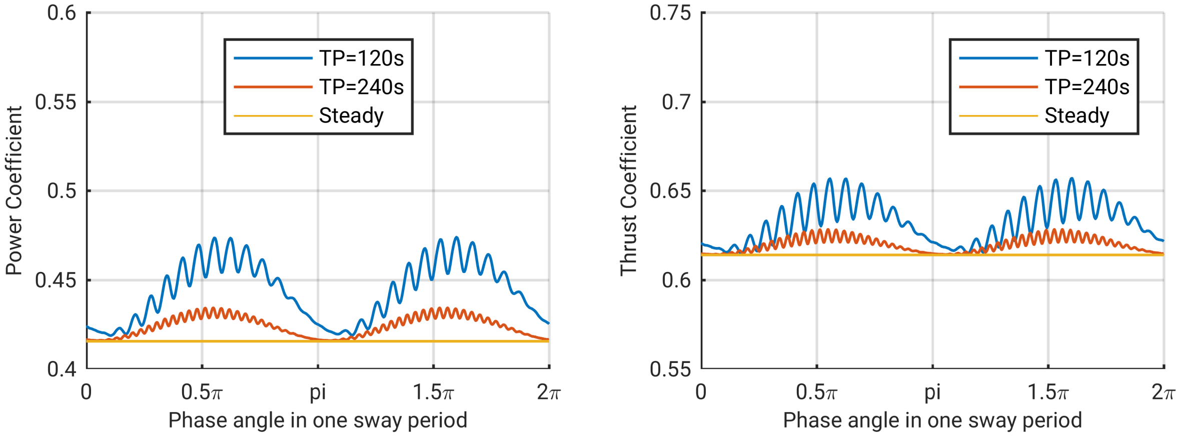

Figure 13: Comparison of power and thrust coefficient of a single rotor DOE RM1 turbine with respect to phase angle in one sway period. TSR=5

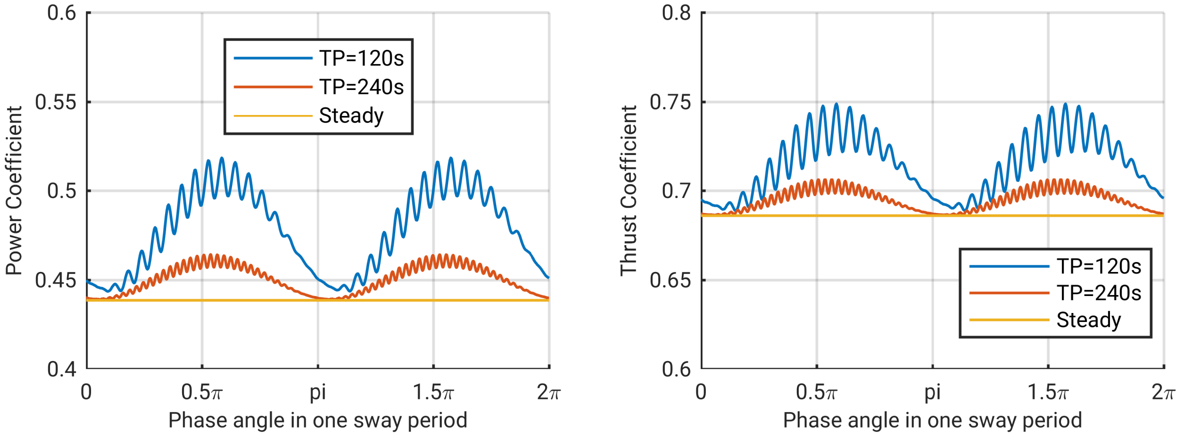

Figure 14: Comparison of power and thrust coefficient of a single rotor DOE RM1 turbine with respect to phase angle in one sway period. TSR=6

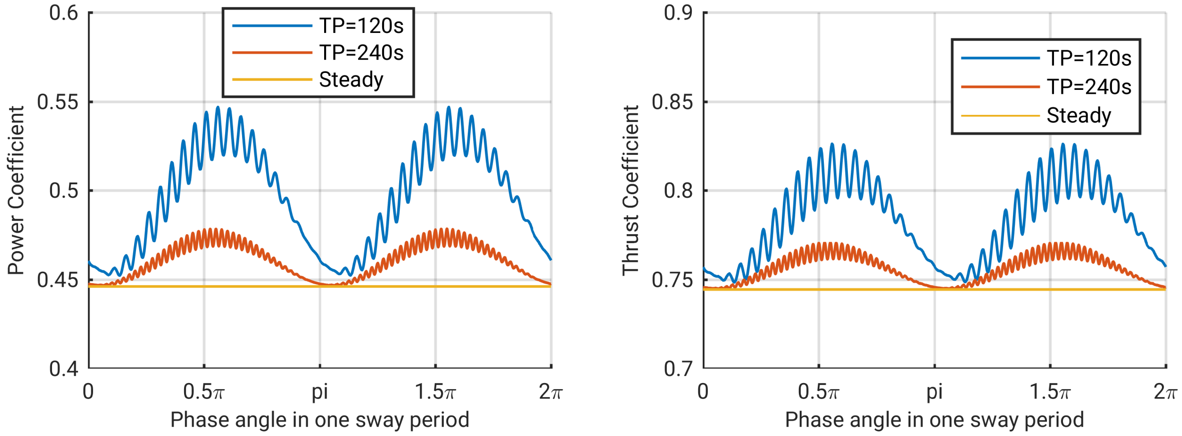

Figure 15: Comparison of power and thrust coefficient of a single rotor DOE RM1 turbine with respect to phase angle in one sway period. TSR=7

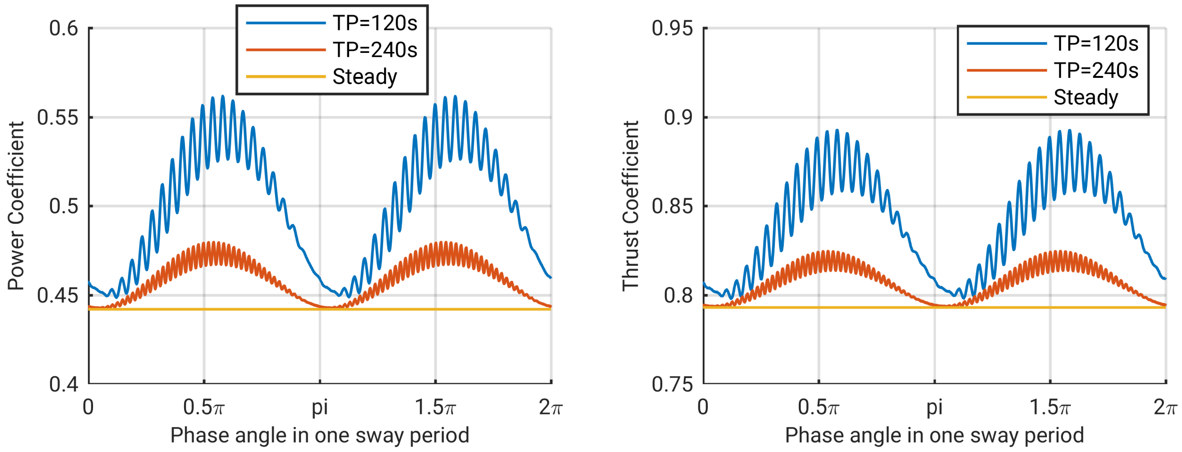

Figure 16: Comparison of power and thrust coefficient of a single rotor DOE RM1 turbine with respect to phase angle in one sway period. TSR=8

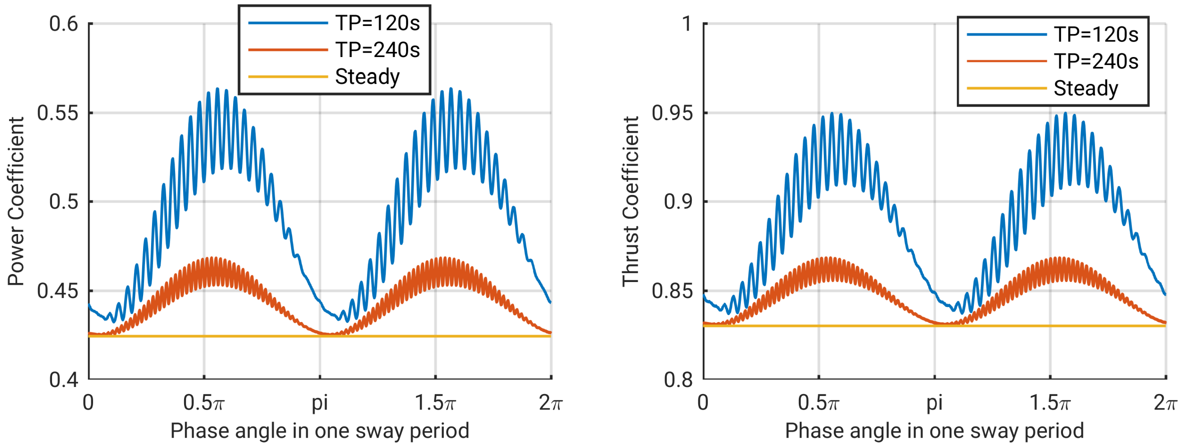

Figure 17: Comparison of power and thrust coefficient of a single rotor DOE RM1 turbine with respect to phase angle in one sway period. TSR=9